ARTICLE

Check for updates

Frenkel-defected monolayer MoS$_2$ catalysts for efficient hydrogen evolution

Jie Xu [1,6], Gonglei Shao[2,3,6], Xuan Tang[4,6], Fang Lv[1], Haiyan Xiang[2], Changfei Jing[5], Song Liu [2✉], Sheng Dai [4✉], Yanguang Li [1✉], Jun Luo [5✉] & Zhen Zhou[3]

Defect engineering is an effective strategy to improve the activity of two-dimensional molybdenum disulfide base planes toward electrocatalytic hydrogen evolution reaction. Here, we report a Frenkel-defected monolayer MoS$_2$ catalyst, in which a fraction of Mo atoms in MoS$_2$ spontaneously leave their places in the lattice, creating vacancies and becoming interstitials by lodging in nearby locations. Unique charge distributions are introduced in the MoS$_2$ surface planes, and those interstitial Mo atoms are more conducive to H adsorption, thus greatly promoting the HER activity of monolayer MoS$_2$ base planes. At the current density of 10 mA cm^{-2}, the optimal Frenkel-defected monolayer MoS$_2$ exhibits a lower overpotential (164 mV) than either pristine monolayer MoS$_2$ surface plane (358 mV) or Pt-single-atom doped MoS$_2$ (211 mV). This work provides insights into the structure-property relationship of point-defected MoS$_2$ and highlights the advantages of Frenkel defects in tuning the catalytic performance of MoS$_2$ materials.

[1] Institute of Functional Nano & Soft Materials (FUNSOM), Jiangsu Key Laboratory for Carbon-Based Functional Materials and Devices, Soochow University, 215123 Suzhou, China. [2] State Key Laboratory of Chemo/Biosensing and Chemometrics, College of Chemistry and Chemical Engineering, Hunan University, 410082 Changsha, Hunan, China. [3] Engineering Research Center of Advanced Functional Material Manufacturing of Ministry of Education, School of Chemical Engineering, Zhengzhou University, 450001 Zhengzhou, China. [4] Feringa Nobel Prize Scientist Joint Research Centre, School of Chemistry and Molecular Engineering, East China University of Science & Technology, 200237 Shanghai, China. [5] School of Materials Science and Engineering, Tianjin Key Lab of Photoelectric Materials & Devices, Tianjin University of Technology, 300384 Tianjin, China. [6] These authors contributed equally: Jie Xu, Gonglei Shao, Xuan Tang. ✉email: liusong@hnu.edu.cn; shengdai@ecust.edu.cn; yanguang@suda.edu.cn; jluo@tjut.edu.cn

The world's growing energy demand based on the finite fossil fuel resources combined with the documented anthropogenic effects on the climate have ignited the research passion for renewable energy technologies. Currently, one area of emphasis is materials and systems for electrocatalytic water splitting (particularly hydrogen evolution reaction, HER) to produce hydrogen as an alternative energy resource due to its high energy density and zero carbon emission in the combustion process[1,2]. An efficient and economical electrocatalyst is the key to achieving significant application for HER. Transition metal dichalcogenides (TMDs) are attracting wide attention due to their low cost and high HER activity. For example, two-dimensional (2D) TMD electrocatalysts are reported to possess enhanced HER performance than that of commercial benchmark Pt/C catalyst at high current densities[3,4], showing great promise in industrial hydrogen production.

As a core member of the TMD material family, 2D molybdenum disulfide (MoS$_2$) materials have been widely used in electrocatalytic HER[5,6]. It is generally considered that their active centers are the unsaturated coordinative atoms at the surface edges, however, the saturated coordinative atoms in the MoS$_2$ surface base planes do not participate in the construction of catalytic active sites, losing the advantage of high specific surface areas of 2D MoS$_2$ to some extent. Thus, several strategies, including defect engineering, surface modification, phase transition engineering, and stress–strain control[7–11], have been proposed to increase the number of active sites on the MoS$_2$ base planes and to optimize their HER performances.

Among them, defect engineering is an efficient measure, and particularly, point defects, e.g., substitution atoms, interstitial atoms, and atomic vacancies, may construct additional active sites in 2D MoS$_2$ toward HER. For instance, the HER performance of 2D MoS$_2$ was greatly improved via introduction of Pt single-atom dopants[7] that modified the coordination environment and charge distribution on the MoS$_2$ surface planes. In addition, Pd single-atom dopants on monolayer 1T-MoS$_2$ were found to activate the planar inert atoms, accelerating the conversion rate to H$_2$[12]. The synergistic effect between the point defects were also revealed to improve the HER performance of MoS$_2$[13–15]. However, current defect engineering strategies on MoS$_2$ are mostly based on heterogeneous atom doping[7,12,14–16], as mentioned above, particularly noble metal doping, which may add the cost and complexity for synthesis approaches. Seeking a facile and economical defect engineering strategy on 2D electrochemical catalysts is of great importance. Meanwhile, the noble metal doping strategy shows limited space for electrocatalytic improvement only on account of the substitution atoms. Whether additional kinds of point defects may provide a desired structure-property relationship for 2D MoS$_2$ is worthwhile exploring.

In this work, by referencing to the native point defects in the text books, we design and synthesize a Frenkel-defected monolayer MoS$_2$ catalyst (denoted as FD-MoS$_2$, including FD-MoS$_2$-3, FD-MoS$_2$-5 and FD-MoS$_2$-15), in which the atomic configuration of the interstitial Mo atoms accompanying with the atomic vacancies is disclosed via aberration-corrected scanning transmission electron microscopy (AC-STEM) and additional spectroscopy characterizations. Micro-reactor electrochemical evaluation shows a significantly enhanced HER activity of the FD-MoS$_2$-5 catalyst, of which the overpotential at the current density of 10 mA cm^{-2} is 164 mV, much lower than those of the reference Pt-single-atom doped monolayer MoS$_2$ plane (211 mV) and the pristine monolayer MoS$_2$ plane (358 mV). Density functional theory (DFT) calculation reveals the unique charge distribution and H adsorption sites introduced by the Frenkel defects in MoS$_2$. These findings highlight the advantages of Frenkel defects in tuning the HER performance of 2D materials for outperforming Pt single-atom doped 2D catalysts.

Results

Synthesis and characterization. In our experiments, pristine monolayer MoS$_2$ was initially prepared by a chemical vapor deposition (CVD) method. Then, the as-prepared MoS$_2$ materials were annealed in Ar atmosphere at 400 °C for 3 min to obtain FD-MoS$_2$-3, as illustrated in Fig. 1a. In addition, the Pt-single-atom doped monolayer MoS$_2$ (denoted as Pt-MoS$_2$) was also prepared via solution spin coating and CVD growth for comparison. Based on the optical microscopy observation, all the three kinds of monolayer MoS$_2$–based materials showed regular triangle shapes (Fig. 1b–d). The thickness of FD-MoS$_2$-3 was measured to be 0.76 nm via atomic force microscopy (AFM) in Supplementary Fig. 1, in accordance with the characteristic of monolayer MoS$_2$ structures[16].

Raman spectroscopy, photoluminescence (PL) spectroscopy, and X-ray photoelectron spectroscopy (XPS) were employed to investigate the structural information of the three MoS$_2$ materials. As shown in the Raman spectra (Fig. 1e), the gap between E^1_{2g} and A_{1g} vibration modes of the pristine MoS$_2$ is ~20 cm^{-1}, the same as that in the previous report[17]. Gauss fitting was used to analyze the full widths at half maximum (FWHM) of the Raman A_{1g} peak of the MoS$_2$, Pt-MoS$_2$, and FD-MoS$_2$-3 samples, and the corresponding values were 8.3, 8.6, and 8.9 cm^{-1}, respectively. The peak broadening of Pt-MoS$_2$ and FD-MoS$_2$-3 samples indicates that they have defective structures[18]. In addition, the Raman peaks of Pt-MoS$_2$ are blue-shifted compared to pristine MoS$_2$, which is related to point defects caused by foreign atom doping[19]. Figure 1f shows the normalized PL spectrum of pristine monolayer MoS$_2$ (normalized to the baseline of PL), and its band gap is ~1.82 eV[20]. As for FD-MoS$_2$-3 and Pt-MoS$_2$, the intensities of the main peaks are significantly suppressed, and both the main peaks show red-shifts. This is due to the change of electron concentration caused by the defect structure, which further confirms the existence of point defects in FD-MoS$_2$-3 and Pt-MoS$_2$[17,21]. We also independently collected the PL data from different regions of MoS$_2$ and FD-MoS$_2$-3 samples, demonstrating that the change of PL spectrum intensity of FD-MoS$_2$-3 relative to MoS$_2$ is reliable (Supplementary Fig. 2).

Moreover, the chemical states of these MoS$_2$ materials were investigated by XPS, as shown in Supplementary Figs. 3 and 4. For the pristine MoS$_2$, the peaks of Mo $3d_{5/2}$ (at 229.7 eV) and $3d_{3/2}$ (at 232.8 eV) are attributed to Mo^{4+}, while the peaks of S $2p_{3/2}$ (at 162.5 eV) and $2p_{1/2}$ (at 163.7 eV) belong to S^{2-}, demonstrating the high quality of as-synthesized pristine MoS$_2$ over a large scale[17]. As for FD-MoS$_2$-3 and Pt-MoS$_2$, the peaks in the Mo $3d$ and S $2p$ regions show high binding-energy shifts, respectively. Such XPS peak shifts of Pt-MoS$_2$ are consistent with a similar case in the literature, indicating the successful doping of Pt atoms in the MoS$_2$ lattice[22].

AC-STEM was carried out to disclose the atomic configurations of these pristine and defected MoS$_2$ materials. Figure 2a shows an overviewing high angle annular dark field (HAADF)-STEM image of the pristine MoS$_2$, in which no obvious point defects (such as S or Mo vacancies) can be observed (more atomic-resolution HAADF-STEM images are provided in Supplementary Fig. 5). An enlarged HAADF-STEM image of the pristine MoS$_2$ (along the <001> zone axis) is presented in Fig. 2b. Here, the high-contrast and low-contrast atoms correspond to Mo and S, respectively, as illustrated by the atomic projection model (Fig. 2c).

An overviewing HAADF-STEM image of FD-MoS$_2$-3 is presented in Fig. 2d (more data are presented in Supplementary Fig. 6). The Frenkel defected sites are highlighted by the yellow arrows. It can be observed that a fraction of Mo atoms leave their own lattice sites, creating Mo vacancies and becoming interstitials by lodging in nearby locations, consistent with the definition of
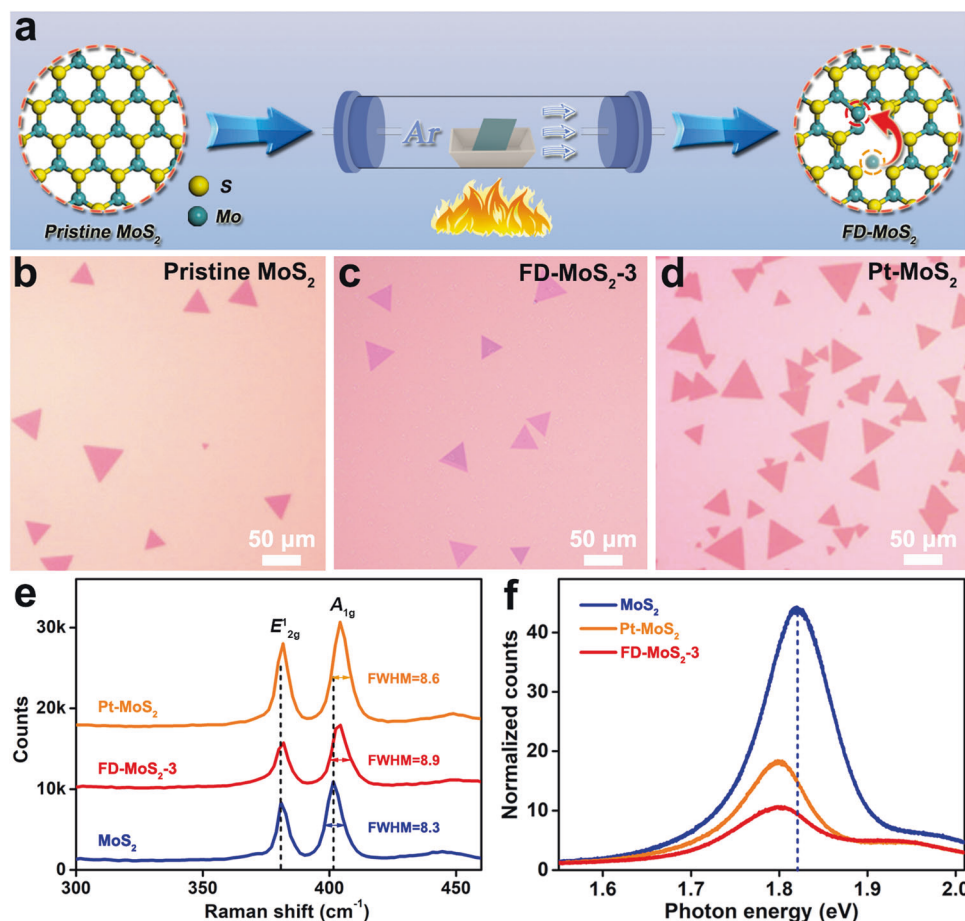
Fig. 1 Preparation and structural characterization of FD-MoS$_2$. a Schematic synthetic procedure for FD-MoS$_2$. **b–d** Typical optical images of monolayer intrinsic MoS$_2$ (**b**), FD-MoS$_2$-3 (**c**), and Pt-MoS$_2$ (**d**). **e**, **f** Raman and normalized PL spectra of the three samples.

Frenkel defects[23]. More atomic-resolution HAADF-STEM images of different regions of FD-MoS$_2$-3 are provided in Supplementary Fig. 7. Importantly, the intermediate state showing the formation of Frenkel defects was captured (Supplementary Fig. 7a, b). The enlarged image (Fig. 2e) illustrates the characteristics of Frenkel defects, and the corresponding atomic model is also presented (Fig. 2f). Accordingly, the S vacancies associated with the Mo Frenkel defects are also identified via elaborate intensity analysis on the Z-contrast HAADF-STEM images (Supplementary Fig. 8). Besides, the existence of S vacancies, but no Mo interstitial, is identified by AC-STEM (Supplementary Fig. 9) in monolayer MoS$_2$ undergoing the Ar annealing for only 1 min. This evidence indicates that the S vacancies should be generated prior to the Mo migration in the formation of Frenkel defects.

In addition, the elapsed time of Ar annealing was extended to investigate its influence on the number of Frankel defects. For example, FD-MoS$_2$-5 was obtained after 5-min Ar annealing and FD-MoS$_2$-15 after 15-min. Compared with FD-MoS$_2$-3, the Raman and PL spectra of FD-MoS$_2$-5 and FD-MoS$_2$-15 show more defect structures (Supplementary Fig. 10)[18,21]. More typical HAADF-STEM images also confirm the increased concentration of Frankel defects in FD-MoS$_2$-5 (Supplementary Fig. 11). However, more holes were observed in addition to the Frenkel defects in FD-MoS$_2$-15 (Supplementary Fig. 12), indicating that the monolayer MoS$_2$ material was unstable and easy to decompose after Ar annealing for a rather long time.

For comparison, Fig. 2g shows the AC-STEM characterization of Pt-MoS$_2$ (the raw data in Supplementary Fig. 13). Pt single atoms in different regions are clearly identified on Pt-MoS$_2$ by

HAADF-STEM imaging (Supplementary Fig. 14). Meanwhile, energy-dispersive X-ray spectroscopy (EDS) elemental maps (Supplementary Fig. 15) confirm the successful and homogeneous doping of Pt atoms. As shown in the HAADF-STEM image and the atomic structure model (Fig. 2h, i), the Pt atoms showing the highest Z-contrast in the image replace the Mo atoms in the MoS$_2$ lattice, constructing a foreign-atom defect type which is different from that in FD-MoS$_2$. Moreover, statistical analysis based on STEM observation, as reported in the previous work[6], is utilized for the defect concentration measurement. As a result, the average concentration of Frenkel defects with the interstitial Mo atoms are measured to be 0.50% and 0.85% in FD-MoS$_2$-3 (Supplementary Fig. 7) and FD-MoS$_2$-5 (Supplementary Fig. 11), respectively, while the average concentration of Pt dopants in Pt-MoS$_2$ is 0.80% (Supplementary Fig. 14).

DFT calculation was performed to investigate the formation process of Frenkel defects in monolayer MoS$_2$. As revealed by the HAADF-STEM evidence (Supplementary Fig. 9), the Frenkel defects (for Mo atoms) were always observed along with the appearance of S vacancies that are easily induced during the Ar annealing process[24,25]. Therefore, it is reasonable that the formation of Frenkel defects in monolayer MoS$_2$ is triggered by those S vacancies. Supplementary Figure 16a–d present the calculated reaction diagrams of monolayer MoS$_2$ with different numbers of S vacancies (e.g., 3, 4, 5, and 6) for the formation of Frenkel defects. As the increase of S vacancy number, the formation energy of Frenkel defects is significantly reduced (Supplementary Fig. 16e), and thermodynamic effects become dominant in the formation of Frenkel defects. Moreover, we
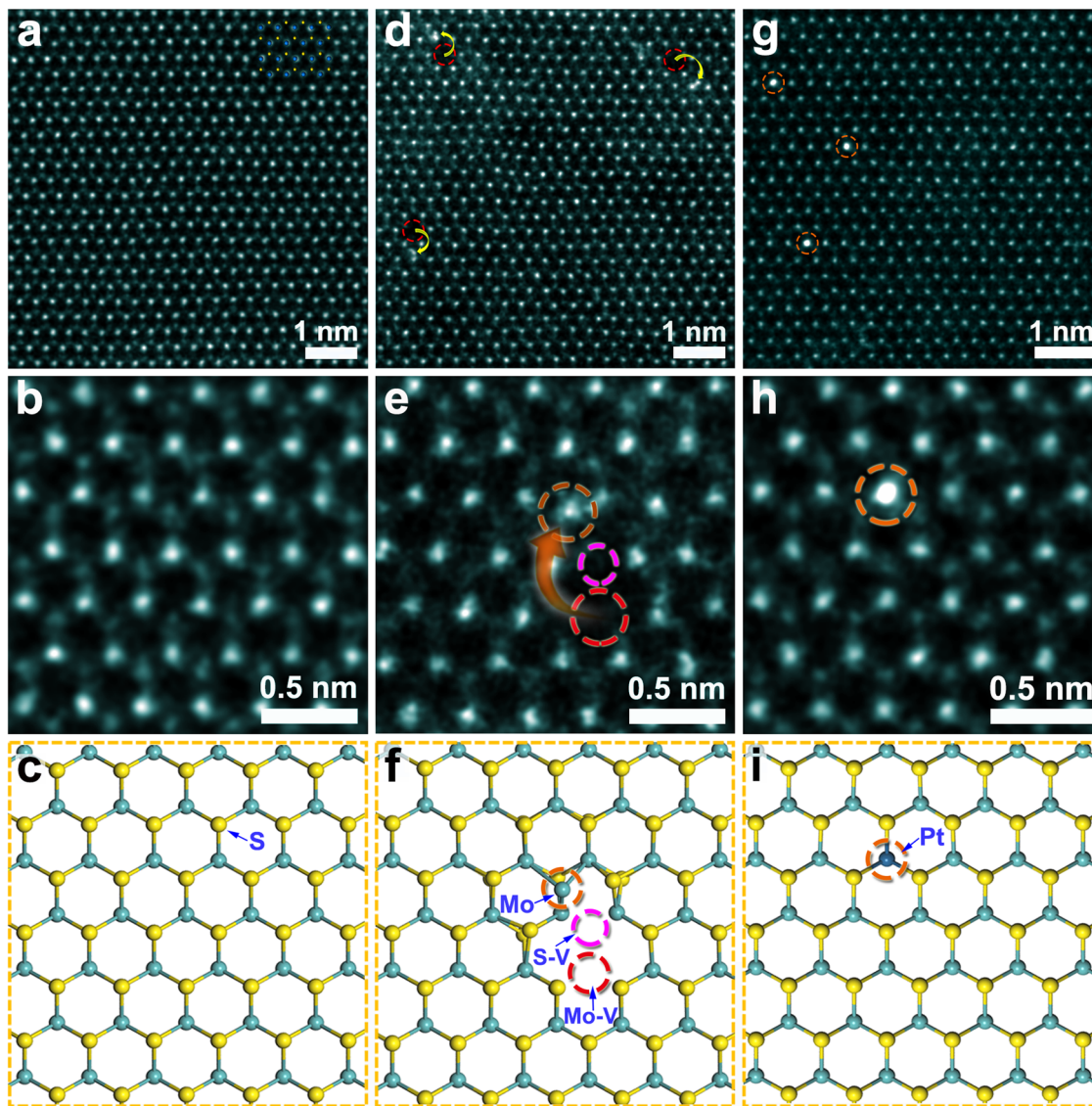
Fig. 2 AC-STEM characterization of MoS₂-based catalysts. Atomic-resolution HAADF-STEM images and corresponding atomic models of monolayer pristine MoS$_2$ (**a–c**), FD-MoS$_2$-3 (**d–f**), and Pt-MoS$_2$ (**g–i**). S-V and Mo-V denote the S and the Mo vacancies, respectively.

calculated the formation energy of different numbers of S vacancies in pristine MoS$_2$ at 673 K (Supplementary Fig. 16f). According to the result, it is feasible to generate S vacancies in the localized regions of MoS$_2$ under our experimental conditions. The presence of S vacancies and the high annealing temperature will easily trigger the migration of Mo atoms to form stable Frenkel defects in MoS$_2$.

Electrocatalytic HER performances. Electrochemical test was then performed to evaluate the HER performances of the monolayer pristine MoS$_2$, Pt-MoS$_2$, FD-MoS$_2$-3, and FD-MoS$_2$-5 catalysts. For conventional electrochemical tests, catalysts are usually loaded on conductive substrates in the form of powders or films. However, for 2D catalysts, the activities of both edges and surface planes are included in this way, and the contributions of the point defects may not be differentiated from those of the unsaturated atoms at edges. To solve this problem, micro-electrochemical devices (Fig. 3a, b) are employed in our set-up[26–28], and only the surface base plane is exposed for the HER evaluation, eliminating the contributions of the edge regions. Meanwhile, the micro-reactor configuration enables an accurate estimation of the electrochemical surface areas (ECSA)

based on the exposed window region and the catalytic activities of simplex 2D surfaces. In order to eliminate the possible dissolution of the Pt electrode affecting the performance[29], a graphite carbon rod was used as the counter electrode (Supplementary Fig. 17) in our set up. Moreover, no H$_2$ bubble generation was found in the exposed windows to block the surface during testing[30].

By comparing the polarization curves of monolayer pristine MoS$_2$, FD-MoS$_2$-3, FD-MoS$_2$-5, and Pt-MoS$_2$, the HER performances of their base planes are shown in Fig. 3c. As revealed, the pristine MoS$_2$ base plane exhibits a quite poor HER activity because of its perfect crystal structure consisting of non-defective six-membered rings that lead to very few active sites, consistent with the previous experimental results[31]. In contrast, FD-MoS$_2$-3, FD-MoS$_2$-5, and Pt-MoS$_2$ show enhanced HER activities than that of pristine MoS$_2$, and particularly, FD-MoS$_2$-5 is even superior, highlighting the advantages of Frenkel-defect engineering strategy on 2D materials.

The overpotential, one of the important indexes to evaluate electrochemical catalytic performances, is used to reflect the difficulty of HER (i.e. the external driving potential required under a rated current density). For example, at the current density of 10 mA cm^{-2}, the base planes of FD-MoS$_2$-3 (174 mV) and
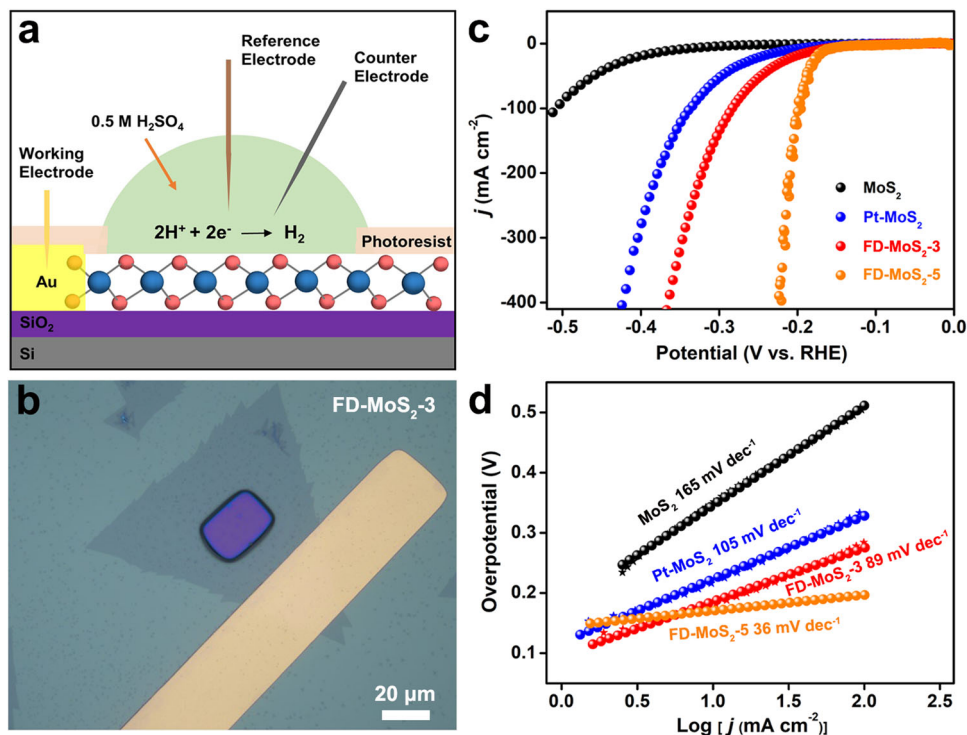
Fig. 3 HER measurement and performance of the MoS$_2$ catalysts by micro-electrochemical devices (micro-reactors). a, b Schematic and optical images of a micro-reactor. The micro-reactors are made by ultraviolet photolithography, and only the surface base plane of MoS$_2$ is exposed in each device. The window area of each type of sample was 450 µm^2 (pristine MoS$_2$), 200 µm^2 (Pt-MoS$_2$), 600 µm^2 (FD-MoS$_2$-3), and 600 µm^2 (FD-MoS$_2$-5). In **b**, the yellow part is an In/Au electrode and the purplish red part is an exposed MoS$_2$ base plane. The edges of the MoS$_2$ samples are all covered by photoresist and did not participate in the HER. **c, d** Polarization curves and Tafel plots of monolayer pristine MoS$_2$, Pt-MoS$_2$, FD-MoS$_2$-3, and FD-MoS$_2$-5 in 0.5 M H$_2$SO$_4$. All current values are normalized by the exposed MoS$_2$ surface areas.

FD-MoS$_2$-5 (164 mV) exhibit lower overpotentials than those of pristine MoS$_2$ (358 mV) and Pt-MoS$_2$ (211 mV). In addition, we further evaluated the HER performance of these materials based on multiple-measurement polarization curves (Supplementary Figs. 18–21). The results confirm that FD-MoS$_2$-5 exhibits the best HER performance. Figure 3d shows the Tafel plots of these MoS$_2$ electrocatalysts that are derived from the corresponding polarization curves[32]. Notably, FD-MoS$_2$-5 (36 mV dec^{-1}) and FD-MoS$_2$-3 (89 mV dec^{-1}) present much smaller Tafel slopes than those of pristine MoS$_2$ (165 mV dec^{-1}) and Pt-MoS$_2$ (105 mV dec^{-1}). Supplementary Figure 22 illustrates the plotting Tafel slopes corresponding to the onset potentials based on statistical analysis, showing that FD-MoS$_2$-5 has the smallest value compared to Pt-MoS$_2$. Considering their similar defect concentrations, this evidence highlights the efficient HER improvement from the Frenkel defects than Pt atom dopants in MoS$_2$. Supplementary Figure 23 also shows the polarization curves of FD-MoS$_2$-15 with more defected structures, whose HER performance was inferior to that of FD-MoS$_2$-5. This indicates that increasing Frenkel defects may not continuously enhance the HER performance, which is also consistent with the results reported in the literature[8,33,34]. Besides, in previously reported works, the overpotential of monolayer MoS$_2$ containing only S vacancies (or only Mo vacancies or both the two types of vacancies) at 10 mA cm^{-2} for HER was found to be ~230 mV (or in a range of 200–300 mV)[35–39], all higher than that of our Frenkel-defected MoS$_2$ catalysts, reflecting the advantages of the Frenkel defects over the Schottky defects in improving HER activities of MoS$_2$ materials. Furthermore, chronoamperometry tests on the FD-MoS$_2$-3 catalyst showed that the monolayer FD-MoS$_2$-3 catalyst may sustain HER for ~10 min (Supplementary Fig. 24), representing a similar stability compared to the pristine monolayer MoS$_2$.

DFT calculations. To gain deeper mechanistic insights into the efficient hydrogen evolution of the point-defected MoS$_2$ catalysts, DFT calculation was performed to reveal the atomic outer valence electron charge density distributions of the models corresponding to monolayer pristine MoS$_2$, FD-MoS$_2$, and Pt-MoS$_2$. As for the pristine MoS$_2$, H is found to be adsorbed on top of the S site in the MoS$_2$ surface plane, as illustrated in Fig. 4a. In contrast, on the surface plane of FD-MoS$_2$, the migration of the Mo atom accompanying with the S vacancy modifies the surface charge distribution and offers additional charges between the S atoms and the Mo atoms adjacent to the original position. Hence, H prefers to adsorb in the vicinity of the interstitial Mo atom, more specifically, between the interstitial Mo atom and the nearby Mo atom (Fig. 4b). The high electron density around S in pristine MoS$_2$ confirms the overly weaker binding for H* again, while the lower electron density around Mo in FD-MoS$_2$ reveals a stronger binding ability. Besides, Fig. 4c presents the charge distribution of Pt-MoS$_2$. The Pt single atoms that substitute the original Mo atoms provide larger charge densities at their exact lattice positions, and H is adsorbed between the Pt atom and the nearby S atom (Fig. 4c). It is illustrated that the charge density distributions of MoS$_2$ change significantly with the introduction of different kinds of point defects, resulting in dissimilar hydrogen adsorption sites.

Furthermore, we compare the HER activities of pristine MoS$_2$, FD-MoS$_2$, and Pt-MoS$_2$ base planes by projected density of states (PDOS) and energy calculations. Figure 4d, e show that the binding of H with the S atom on pristine monolayer MoS$_2$ is quite weak, and the corresponding Gibbs free energy is 2.03 eV, indicating a difficult Volmer process and a poor activity for HER on well-defined MoS$_2$ base plane. In contrast, a much stronger binding of H-S (−1.09 eV) is obtained on Pt-MoS$_2$, where the
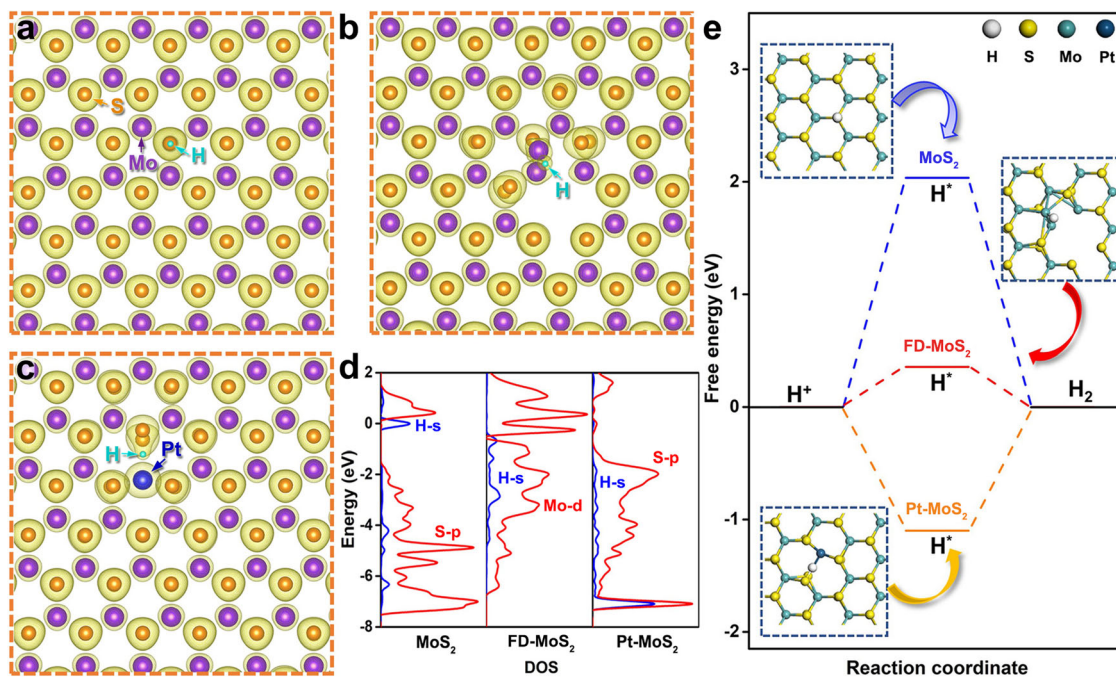
Fig. 4 DFT calculation results of the surface charge density distributions and HER catalytic activities of monolayer pristine MoS$_2$, FD-MoS$_2$, and Pt-MoS$_2$. a–c Calculated surface charge distributions when H is adsorbed on monolayer pristine MoS$_2$, FD-MoS$_2$, and Pt-MoS$_2$, respectively. **d** Calculated PDOS of active site and H on the different catalyst surfaces. **e** Free energy diagrams of HER on the three MoS$_2$ catalysts.

electronic resonance from PDOS can be found at a lower energy level in Fig. 4d. Note that, the S-Pt bond is found to be broken with the adsorbed H on Pt-MoS$_2$. Importantly, the adsorption energy of H* on Mo in FD-MoS$_2$ is calculated to be 0.36 eV, implying a moderate and suitable binding energy for HER on the studied surfaces. In addition, we further analyzed the different active sites in FD-MoS$_2$, and the results showed that interstitial Mo atoms are the optimal HER active centers (Supplementary Fig. 25). Therefore, based on the DFT calculation, the HER activity of the MoS$_2$ models should follow the sequence, FD-MoS$_2$ > Pt-MoS$_2$ > MoS$_2$, consistent with our experimental evidence. Meanwhile, we also calculated the H* adsorption energy of FD-MoS$_2$ with different defect concentrations (Supplementary Fig. 26), and the results indicated that a little bit higher concentrations may be beneficial to the HER catalytic activity, in agreement with our experimental results of FD-MoS$_2$-3 and FD-MoS$_2$-5 (Fig. 3c, d). Besides, we further analyzed the partial electron density distribution of the Frankel defect structure in MoS$_2$ (Supplementary Fig. 27). The formation of Frankel defects causes more electrons to gather in its vicinity, making the defects become active sites for catalyzing the HER.

Discussion

In summary, a Frenkel-defected monolayer MoS$_2$ catalyst has been designed and synthesized via a facile Ar annealing treatment, and the atomic configurations of the Frenkel defects in MoS$_2$ are revealed by AC-STEM observation. According to the electrochemical test employing the micro-reactor, FD-MoS$_2$ shows an enhanced HER activity compared to the pristine MoS$_2$ and Pt-MoS$_2$ catalysts. DFT calculation reveals the unique charge distribution introduced by the existence of Frenkel defects in MoS$_2$, which change the H adsorption site and provide a moderate adsorption energy of H* for FD-MoS$_2$. This work not only gains insight into the structure-property relationships of point-defected MoS$_2$ materials, but also provides an efficient and economical defect engineering strategy over 2D electrochemical catalysts at atomic level.

Methods

Chemicals. The SiO$_2$/Si (270 nm SiO$_2$) substrates were purchased from Suzhou Ruicai Semiconductor Co., Ltd.; MoO$_3$ (≥99.5%) and S powder (≥99.5%) were purchased from Sigma-Aldrich (Shanghai) Trading Co., Ltd.; NaCl (≥99.5%), chloroplatinic acid and sodium molybdate (99.0%) were purchased from Shanghai Aladdin Biochemical Technology Co., Ltd.

Synthesis of monolayer pristine MoS$_2$. Firstly, the SiO$_2$/Si substrates were cleaned by following the sequence of using piranha solution, isopropanol, and DI water[40]. Then MoO$_3$ (15 mg) and NaCl (3 mg) were mixed and placed in the middle of an aluminum trioxide crucible. The SiO$_2$/Si substrate (size: 1 × 2 cm) was located above the powders, and the crucible was placed in the middle of a quartz tube in the CVD furnace. Sulfur powder (320 mg) was placed in another crucible in upstream, ~15 cm away from the middle of the furnace. The system was firstly ventilated with Ar (300 sccm) for 10 min for flushing, and then Ar (100 sccm) was maintained to flow in the system. The furnace was heated up to 705 °C in 40 min, and then maintained at 705 °C for 5 min. At the end, the CVD furnace was cooled to room temperature naturally.

Synthesis of monolayer FD-MoS$_2$. The grown pristine MoS$_2$ was placed in the middle of an additional quartz tube. The system was first ventilated with Ar (300 sccm) for 10 min to remove the impurities in the tube, and the inert atmosphere was maintained with Ar (100 sccm) to flow in the system. Then, the furnace was heated to the specified temperature (400 °C) within 60 min in this atmosphere, and kept at 400 °C for 3 min. Finally, the CVD furnace was slowly cooled to room temperature. The synthesis conditions of FD-MoS$_2$-5 and FD-MoS$_2$-15 are similar to that of FD-MoS$_2$-3, except the extended annealing time of 5 and 15 min, respectively.

Synthesis of monolayer Pt-MoS$_2$. Pt-doped MoS$_2$ was obtained according to our previously reported method by the following steps[41]. First, 995 μL of Na$_2$MoO$_4$ (10 mmol) and 5 μL of H$_2$PtCl$_6$ (24.4 mmol) were mixed to form a precursor solution. Fresh SiO$_2$/Si substrates were treated under oxygen plasma (60 W) for 1 min (CIF Tech Co., Ltd. CPC-C-40 KHz). The precursor solution was spin-coated onto the treated substrates at 3000 rpm for 1 min. Then, the substrate with precursor was loaded into the center of the furnace. A crucible with sulfur powder (150 mg) was located at upstream, 15 cm away from the middle of the furnace. Ar (270 sccm) was used as carrying gas, and the growth temperature was gradually raised to 850 °C in 40 min. The sulfur powder was subsequently pushed into the hot zone and kept for 5 min at 850 °C. Then the CVD furnace was slowly cooled to room temperature.

Structural characterization. The morphologies of these 2D samples were observed by optical microscopy (Nikon H600L) and atomic force microscope

(AFM, Bruker Dimension Icon). Raman and PL spectra were obtained by Horiba Instruments INC (1024×256-OE) equipped with a 532 nm laser excitation and a CCD detector in a backscattering geometry. The XPS data of these 2D samples on the SiO₂/Si substrates were analyzed by ESCALAB 250Xi X-ray photoelectron spectroscopy equipped with a monochromatic Al Kα source ($\lambda = 1486.6$ eV). The ~284.8 eV adventitious C 1 s peak was used for charging corrections. The AC-STEM characterization was performed using a ThermoFisher Themis Z microscope equipped with two aberration correctors under 300 kV.

Device fabrication. According to our previous device fabrication method[41], the SiO₂/Si substrates with different 2D products were spin-coated with SPR-220-3a photoresist at 4000 rpm for 1 min, and then baked at 115 °C for 90 s. Next, the SiO₂/Si substrates covered with photoresist were patterned for electrode pattern by ultraviolet, and then deposited with In/Au (10 nm/50 nm) by thermal evaporation to connect the monolayer 2D samples. Residual photoresist was removed by acetone following a lift-off process, and the metallic electrode patterns were obtained for devices. In the microelectrocatalytic process, photoresist was spin-coated again on the evaporated devices in SiO₂/Si substrates, and baked at 115 °C for 90 s. And then these 2D samples exposed with proper ultraviolet beam to open windows (the actual surface area of the exposed 2D materials) on the target positions of the monolayer samples for HER measurements.

HER measurements. The micro-electrocatalysis performance was tested by a three-electrode system using a CHI 660E electrochemical workstation. Graphite carbon electrode with a diameter of 1 mm tip served as the count electrode, and a homemade saturated Ag/AgCl electrode served as the reference electrode. The exposed area of each measured monolayer 2D samples served as the working electrode. The HER activity of each monolayer was evaluated in 0.5 M H₂SO₄ electrolyte by linear sweep voltammetry at a scan rate of 5 mV s⁻¹. The volume of the droplets on the window surface of the 2D material was fixed at 5 µL. All reported potentials were converted to reversible hydrogen electrode (RHE) potentials, and no iR-corrected was used in all the electrochemical measurements.

Computational methods. DFT calculation was performed using the Vienna ab initio simulation package (VASP)[42]. The Generalized Gradient Approximation (GGA)[43] with the Perdew–Burke–Ernzerhof (PBE) functional was used for all the calculations. HER performance and fundamental electronic characters were studied over the three different catalysts, including monolayer pristine MoS₂, Pt-MoS₂ and FD-MoS₂. Each of the structures was built based on a periodic 6 × 6 single layer MoS₂ surface with 36 Mo atoms and 72 S atoms (up to 144 Mo atoms and 288 S atoms were built). A Monkhorst-Pack k-point 2 × 2 × 1 was used for all the surface calculations with the cut-off energy of 400 eV. The structural optimization was conducted using the conjugate-gradient (CG) algorithm[44], and the force convergence was set to be 0.05 eV·Å⁻¹. The standard free energies correction[45] was used to obtain the free energy at 298 K, following $\triangle G = \triangle E + \triangle ZPE + \triangle U - T\triangle S$, where G, E, ZPE, U, T, and S refer to the free energy, total energy, zero-point energy, inner energy, temperature and entropy, respectively. In addition, electrical neutrality was considered in all DFT calculations. Notably, due to the large size of the MoS₂ model, only GGA could be utilized here. Generally, more accurate electronic structure information could be calculated by using a higher-precision or hybrid functional.

Data availability

All data supporting the findings of this study are available from the Source Data. Source data are provided with this paper.

References

1. Ran, J., Zhang, J., Yu, J., Jaroniec, M. & Qiao, S. Z. Earth-abundant cocatalysts for semiconductor-based photocatalytic water splitting. *Chem. Soc. Rev.* **43**, 7787–7812 (2014).
2. Xu, J. et al. Amorphous MoO_X-stabilized single platinum atoms with ultrahigh mass activity for acidic hydrogen evolution. *Nano Energy* **70**, 104529 (2020).
3. Yang, J. et al. Ultrahigh-current-density niobium disulfide catalysts for hydrogen evolution. *Nat. Mater.* **18**, 1309–1314 (2019).
4. Zheng, Z. et al. Boosting hydrogen evolution on MoS₂ via co-confining selenium in surface and cobalt in inner layer. *Nat. Commun.* **11**, 3315 (2020).
5. Zhou, Y. et al. Enhanced performance of in-plane transition metal dichalcogenides monolayers by configuring local atomic structures. *Nat. Commun.* **11**, 2253 (2020).
6. Luo, Y. et al. Unsaturated single atoms on monolayer transition metal dichalcogenides for ultrafast hydrogen evolution. *ACS Nano* **14**, 767–776 (2020).
7. Deng, J. et al. Triggering the electrocatalytic hydrogen evolution activity of the inert two-dimensional MoS₂ surface via single-atom metal doping. *Energy Environ. Sci.* **8**, 1594–1601 (2015).
8. Wang, X. et al. Single-atom vacancy defect to trigger high-efficiency hydrogen evolution of MoS₂. *J. Am. Chem. Soc.* **142**, 4298–4308 (2020).
9. Voiry, D., Yang, J. & Chhowalla, M. Recent strategies for improving the catalytic activity of 2D TMD nanosheets toward the hydrogen evolution reaction. *Adv. Mater.* **28**, 6197–6206 (2016).
10. Li, Y. et al. Synergistic Pt doping and phase conversion engineering in Two-dimensional MoS₂ for efficient hydrogen evolution. *Nano Energy* **84**, 105898 (2021).
11. Zang, Y. et al. Tuning orbital orientation endows molybdenum disulfide with exceptional alkaline hydrogen evolution capability. *Nat. Commun.* **10**, 1217 (2019).
12. Lau, T. H. M. et al. Engineering monolayer 1T-MoS₂ into a bifunctional electrocatalyst via sonochemical doping of isolated transition metal atoms. *ACS Catal.* **9**, 7527–7534 (2019).
13. Zhang, H., Yu, L., Chen, T., Zhou, W. & Lou, X. W. Surface modulation of hierarchical MoS₂ nanosheets by Ni single atoms for enhanced electrocatalytic hydrogen evolution. *Adv. Funct. Mater.* **28**, 1807086 (2018).
14. Jiang, K. et al. Rational strain engineering of single-atom ruthenium on nanoporous MoS₂ for highly efficient hydrogen evolution. *Nat. Commun.* **12**, 1687 (2021).
15. Zhang, J., Xu, X., Yang, L., Cheng, D. & Cao, D. Single-atom Ru doping induced phase transition of MoS₂ and S vacancy for hydrogen evolution reaction. *Small Methods* 3, 1900653 (2019).
16. Duan, H. et al. Single-atom-layer catalysis in a MoS₂ monolayer activated by long-range ferromagnetism for the hydrogen evolution reaction: beyond single-atom catalysis. *Angew. Chem. Int. Ed.* **60**, 7251–7258 (2021).
17. Zhang, X. et al. Hidden vacancy benefit in monolayer 2D semiconductors. *Adv. Mater.* **33**, 2007051 (2021).
18. Zhu, J. et al. Argon plasma induced phase transition in monolayer MoS₂. *J. Am. Chem. Soc.* **139**, 10216–10219 (2017).
19. Zhou, Y. et al. Enhanced performance of in-plane transition metal dichalcogenides monolayers by configuring local atomic structures. *Nat. Commun.* **11**, 2253 (2020).
20. Shao, G. et al. Seamlessly splicing metallic Sn_xMo₁₋_xS₂ at MoS₂ edge for enhanced photoelectrocatalytic performance in microreactor. *Adv. Sci.* **7**, 2002172 (2020).
21. Mak, K. F. et al. Tightly bound trions in monolayer MoS₂. *Nat. Mater.* **12**, 207–211 (2013).
22. Shao, G. et al. Template-assisted synthesis of metallic 1T′-Sn₀.₃W₀.₇S₂ nanosheets for hydrogen evolution reaction. *Adv. Funct. Mater.* **30**, 1906069 (2020).
23. De Villiers, J. P. R. & Buseck, P. R. *Encyclopedia of Physical Science and Technology*. 3rd edn (Elsevier Science Ltd., 2003).
24. Yang, S. et al. Unique three-dimensional Mo₂C@MoS₂ heterojunction nanostructure with S vacancies as outstanding all-pH range electrocatalyst for hydrogen evolution. *J. Catal.* **371**, 20–26 (2019).
25. You, M. et al. High temperature induced S vacancies in natural molybdenite for robust electrocatalytic nitrogen reduction. *J. Colloid Interface Sci.* **599**, 849–856 (2021).
26. Yu, Y. et al. High phase-purity 1T′-MoS₂- and 1T′-MoSe₂-layered crystals. *Nat. Chem.* **10**, 638–643 (2018).
27. Zhu, J. et al. Boundary activated hydrogen evolution reaction on monolayer MoS₂. *Nat. Commun.* **10**, 1348 (2019).
28. Zhang, J. et al. Unveiling active sites for the hydrogen evolution reaction on monolayer MoS₂. *Adv. Mater.* **29**, 1701955 (2017).
29. Chen, J. G., Jones, C. W., Linic, S. & Stamenkovic, V. R. Best practices in pursuit of topics in heterogeneous electrocatalysis. *ACS Catal.* **7**, 6392–6393 (2017).
30. Chen, Q., Luo, L., Faraji, H., Feldberg, S. W. & White, H. S. Electrochemical measurements of single H₂ nanobubble nucleation and stability at Pt nanoelectrodes. *J. Phys. Chem. Lett.* **5**, 3539–3544 (2014).
31. Zhang, P. et al. Chemically activated MoS₂ for efficient hydrogen production. *Nano Energy* **57**, 535–541 (2019).
32. Chung, D. Y. et al. Electrokinetic analysis of poorly conductive electrocatalytic materials. *ACS Catal.* **10**, 4990–4996 (2020). 9.
33. Xie, J. et al. Controllable disorder engineering in oxygen-incorporated MoS₂ ultrathin nanosheets for efficient hydrogen evolution. *J. Am. Chem. Soc.* **135**, 17881–17888 (2013).
34. Cheng, C. C. et al. Activating basal-plane catalytic activity of two-dimensional MoS₂ monolayer with remote hydrogen plasma. *Nano Energy* **30**, 846–852 (2016).
35. Voiry, D. et al. The role of electronic coupling between substrate and 2D MoS₂ nanosheets in electrocatalytic production of hydrogen. *Nat. Mater.* **15**, 1003–1009 (2016).
36. Li, H. et al. Activating and optimizing MoS₂ basal planes for hydrogen evolution through the formation of strained sulphur vacancies. *Nat. Mater.* **15**, 48–53 (2016).

37. Tsai, C. et al. Electrochemical generation of sulfur vacancies in the basal plane of MoS$_2$ for hydrogen evolution. *Nat. Commun.* **8**, 15113 (2017).
38. Kong, C., Zhang, F., Wang, Y. & Huang, J. Synthesis and photocatalytic hydrogen activity of Mo$_{1-x}$S$_2$ nanosheets with controllable Mo vacancies. *J. Alloy. Compd* **876**, 160165 (2021).
39. Yang, J. et al. Single atomic vacancy catalysis. *ACS Nano* **13**, 9958–9964 (2019).
40. Shao, G. et al. Twist angle-dependent optical responses in controllably grown WS$_2$ vertical homojunctions. *Chem. Mater.* **32**, 9721–9729 (2020).
41. Xiang, H. et al. Self-gating enhanced carrier transfer in semiconductor electrocatalyst verified in microdevice. *Chin. Chem. Lett.* https://doi.org/10.1016/j.cclet.2021.10.033 (2021).
42. Kresse, G. & Hafner, J. Ab initio molecular-dynamics simulation of the liquid-metal–amorphous-semiconductor transition in germanium. *Phys. Rev. B* **49**, 14251 (1994).
43. Perdew, J. P., Burke, K. & Ernzerhof, M. Generalized gradient approximation made simple. *Phys. Rev. Lett.* **78**, 1396 (1997).
44. Hestenes, M. R. & Stiefel, E. Methods of conjugate gradients for solving linear systems. *J. Res. Natl Bur. Stand.* **49**, 409 (1952).
45. Cao, X. M., Burch, R., Hardacre, C. & Hu, P. An understanding of chemoselective hydrogenation on crotonaldehyde over Pt (111) in the free energy landscape: the microkinetics study based on first-principles calculations. *Catal. Today* **165**, 71–79 (2011).

Author contributions

J.L., S.D., and J.X. conceived and designed the project. G.S. and S.L. performed the synthetic and electrochemical experiments, to which F.L., H.X., and Z.Z. contributed. J.X., X.T., and C.J. performed the electron microscopy experiment. J.X. and G.S. analyzed the experimental data. J.X., J.L., and S.D. wrote the manuscript. J.L., Y.L., S.D., and S.L. supervised the project. All authors discussed the results.

Competing interests

The authors declare no competing interests.

Additional information

Supplementary information The online version contains supplementary material available at https://doi.org/10.1038/s41467-022-29929-7.

Correspondence and requests for materials should be addressed to Song Liu, Sheng Dai, Yanguang Li or Jun Luo.

Peer review information *Nature Communications* thanks Scott Misture and the other, anonymous, reviewer(s) for their contribution to the peer review of this work.

Reprints and permission information is available at http://www.nature.com/reprints

Publisher's note Springer Nature remains neutral with regard to jurisdictional claims in published maps and institutional affiliations.